

Cite this: *J. Mater. Chem. C*, 2023,
11, 2282Air-stable high-PLQY cesium lead halide
perovskites for laser-patterned displays†Ping Liu,^{‡ab} Boyang Yu,^{id ‡c} Wanqing Cai,^{id ‡*d} Xiongqian Yao,^{ab} Kai Chang,^c
Xinyan Zhao,^{id c} Zhichun Si,^{id b} Weiwei Deng,^{id *c} Yuanyuan Zhou,^{id *ef}
Guangmin Zhou^{id *ab} and Guodan Wei^{id *ab}

Metal halide perovskites (MHPs) have emerged as attractive building blocks for advanced photoluminescence display applications. But the practical deployment of MHP displays is hindered by the relatively low air stability, which can cause difficulty in high-precision film patterning under ambient conditions while achieving high photoluminescence quantum yields (PLQYs). Here we incorporate a polymer additive of poly(2-ethyl-2-oxazoline) (PEtOx) in the solution processing of quasi-2D phenylbutylamine bromide/cesium lead halide (PBABr/CsPbBr_{0.6}I_{2.4}) perovskite films, which not only results in a high PLQY of 91%, but more importantly improves the ambient stability *via* Lewis base–acid interaction of oxygen functional groups of the polymer and Pb of the perovskite. Using time-resolved optical spectroscopy and femtosecond transient absorption spectroscopy, we find that in the PEtOx-stabilized quasi-2D perovskite film, the trap-assisted nonradiative recombination rate is reduced while the radiative recombination is significantly promoted, underpinning the PLQY improvements. *Via* maskless laser direct-write patterning onto this air-stable high-PLQY perovskite film, we have achieved complex-patterned displays on both rigid and flexible substrates, with anti-counterfeiting encryption code as a proof-of-concept demonstration. This work opens new opportunities for engineering perovskites to multifunctional display applications.

Received 19th October 2022,
Accepted 6th January 2023

DOI: 10.1039/d2tc04445e

rsc.li/materials-c

Introduction

Advanced photoluminescence displays are important in the area of anti-counterfeiting and information encryption, and searching for stable and efficient phosphor materials is the key to their commercial development. In the past years, carbon

quantum dot materials¹ and lanthanide luminescent inks² have been mostly explored, but there are intrinsic drawbacks associated with these materials. For instance, carbon dots suffer from low fluorescence efficiency and poor color purity, making them easy to be duplicated. The costs of lanthanide materials are relatively high, rendering it difficult to apply them in large-scale anti-counterfeiting scenarios such as paper money. Recently, metal halide perovskites have emerged as an attractive material system for photoluminescence applications. In particular, their photoluminescent properties have been attested by their superior applications in a range of optoelectronic devices such as solar cells, light-emitting diodes (LEDs), photodetectors, and lasers.³

For advanced display applications, perovskites exhibit various desirable properties, including tunable photo-emission, extended visible range activities, and high PLQYs. There have been a handful of efforts combining perovskite materials with conventional patterning technologies for anti-counterfeiting and information encryption applications.⁴ However, the poor air-stability remains one of the main obstacles for their practical application. Also, with regard to perovskite patterning, the conventional methods used are mostly lithography and inkjet printing.⁵ The former involves complex masking procedures and solvents for lithographic patterning.⁵ The latter relies on specially formulated perovskite

^a Tsinghua-Berkeley Shenzhen Institute (TBSI), Tsinghua University, Shenzhen 518055, China. E-mail: weiguodan@sz.tsinghua.edu.cn, guangminzhou@sz.tsinghua.edu.cn, liuping19@mails.tsinghua.edu.cn, yaoux21@mails.tsinghua.edu.cn

^b Institute of Materials Science, Tsinghua Shenzhen International Graduate School, Tsinghua University, Shenzhen 518055, China. E-mail: si.zhichun@sz.tsinghua.edu.cn

^c Department of Mechanics and Aerospace Engineering, Southern University of Science and Technology (SUSTech), Shenzhen 518055, China. E-mail: dengww@sustech.edu.cn, 11930344@mail.sustech.edu.cn, changkai.work@foxmail.com, zhaoxy@sustech.edu.cn

^d Faculty of Materials Science, MSU-BIT University, Shenzhen 518172, China. E-mail: wqcai@smbu.edu.cn

^e Department of Applied Physics, The Hong Kong Polytechnic University, Hong Kong SAR, 999077, China. E-mail: yyzhou@hkbu.edu.hk

^f Smart Society Laboratory, Hong Kong Baptist University, Kowloon, Hong Kong SAR, 999077, China

† Electronic supplementary information (ESI) available. See DOI: <https://doi.org/10.1039/d2tc04445e>

‡ These three authors contributed equally.



inks with controlled viscosities and surface tensions, and the precision of patterning resulting from this solution process is limited.⁷ In this context, it remains challenging to obtain high-precision patterned perovskite films in ambient air without the use of masking,^{4b,8} which calls for the needs of both developing air-stable high-PLQY perovskite films and unconventional patterning methods.

In this work, by performing mask-less laser direct-write patterning onto this high-PLQY air-stable perovskite film, we achieved rigid and flexible complex patterned displays, with anti-counterfeiting encryption code as proof-of-concept demonstration. We demonstrated efficient and air-stable pure-red quasi-2D perovskite thin films based on PETOx polymer engineering *via* one-step spin-coating. Under optimized experimental conditions, the quasi-2D perovskite films yielded a single emission peak at 634 nm with a remarkable PLQY value of over 90%, which is among the best reported performance for quasi-2D pure-red perovskite thin films to date (Table S1, ESI†). PETOx was used as a cross-linked polymer to form PBABr/CsPbBr_{0.6}I_{2.4} perovskite/PETOx composite thin films. As reported in a previous work,⁹ the oxygen atoms in the PETOx were strongly coordinated with Pb²⁺ in the form of a Lewis base–acid interaction, forming Lewis adducts with PbI₂ through Pb–O bonds,¹⁰ thus enhancing the air stability and suppressing the humidity effect. It is well-known that photoluminescence (PL) efficiency is highly dependent on the competition between radiative (k_{rad}) and non-radiative (k_{nonrad}) recombination rates. Therefore, detailed investigation and direct experimental support are provided in our work to reveal the underlying mechanisms of high PLQYs in PETOx treated perovskite thin films. The simple laser direct-write patterning procedure used here is a convenient and effective technique for large-area fabrication without any demand of a vacuum environment, high temperature, or complicated post-processing. No solvent or lift-off procedure is needed, thus avoiding the dissolution problem of perovskites in common polar solvents. The excellent optoelectronic properties of perovskite materials are preserved throughout the fabrication process. Our work demonstrates the great potential of this high PLQY perovskite for photoluminescence display applications and may pave the way for exploration of perovskite micro- and nanoscale light emitting devices.

Results and discussion

The process of preparing light emitting quasi-2D perovskite/PETOx films *via* laser direct-write patterning is shown in Fig. S1 (ESI†). Typically, 3D CsPbBr_{0.6}I_{2.4} perovskite solutions were prepared by mixing CsPbI₃ and CsPbBr₃ precursor solutions with a 4 : 1 volume ratio. Organic salt phenylbenzyl ammonium bromide (PBABr) was added to the CsPbBr_{0.6}I_{2.4} solutions with a certain molar ratio of 0.6 : 1 to synthesize quasi-2D PBABr/CsPbBr_{0.6}I_{2.4}. To achieve the goal of obtaining high-quality and stable perovskite films with high PLQYs, we introduced polymer PETOx additives into the 3D CsPbBr_{0.6}I_{2.4} precursor solution to assist the growth of perovskite crystals

in PBABr/CsPbBr_{0.6}I_{2.4}/PETOx composite thin films. The detailed results of PLQY optimization of the composite films by varying the molar ratio of PBABr, weight ratio of PETOx and annealing temperature are shown in Fig. S2, ESI.† Considering the 91% PLQY and a dominant PL peak at 634 nm, we chose 0.6 molar ratio of PBABr and 20% weight ratio of PETOx as the optimal ratio for the composite films. All perovskite thin films were prepared by spin coating the mixture solutions evenly at 4000 rpm for 45 s onto the glass substrate, followed by thermal annealing at 110 °C for 10 min to promote the crystallization. Subsequently, we use laser direct-write patterning to obtain the fine patterns of stable perovskite films, as described in the Experimental section.

The X-ray diffraction (XRD) spectra of all samples shown in Fig. 1a confirm the formation of CsPbI₃ perovskites with stable crystalline black phase. By contrast, thin film PBABr/CsPbBr_{0.6}I_{2.4} shows various strong diffraction peaks at 12°, 14.5° and 29°, verifying a better quasi-2D layered crystallinity with small n (n = the number of PbI₄ perovskite layers). In addition, for thin film PBABr/CsPbBr_{0.6}I_{2.4}/PETOx, the diffraction peaks at around 14.5° and 29.0° reveal (100) and (200) crystalline planes of black phase CsPbI₃, respectively, while no obvious diffraction peaks corresponding to layered quasi-2D perovskites are observed.¹¹ This indicates the formation of quasi-2D perovskite thin films with large n for PBABr/CsPbBr_{0.6}I_{2.4}/PETOx. To investigate the effects of PETOx polymer additives on the morphology of quasi-2D perovskite thin films, SEM and AFM measurements were performed, and the statistical data are shown in Table S2 (ESI†). As exhibited in Fig. 1b–d, the introduction of PETOx additives onto quasi-2D perovskites can substantially improve the surface coverage of films, showing a decreased grain size and increased number density of grains. We can clearly observe that the PETOx-treated sample has the smallest grain size. The reduced grain size implies an enhanced exciton confinement, thus an increased PLQY can be expected.¹² Meanwhile, the root-mean-square roughness (R_a) of the perovskite thin films was extracted from the AFM results, shown in Fig. 1e–g. We can see that the R_a value of the PBABr/CsPbBr_{0.6}I_{2.4}/PETOx sample is about 2.75 nm, which is much lower than that of the control sample (9.83 nm, shown in Fig. S3, ESI†), demonstrating the improved quality of the thin films. In a word, the improved surface coverage, reduced grain size, and decreased surface roughness together confirm the positive effect of PETOx treatment on the morphology quality of quasi-2D perovskite films, suggesting their application potential for light-emitting displays and devices.

Furthermore, we explored the optical properties of the light emitting PBABr/CsPbBr_{0.6}I_{2.4}/PETOx composite thin films. As depicted in Fig. 2a, thin film PBABr/CsPbBr_{0.6}I_{2.4}/PETOx possess pure-red emission at 634 nm, which is analogous to thin film PBABr/CsPbBr_{0.6}I_{2.4}, demonstrating that the addition of PETOx will not change the composition and crystallinity of quasi-2D perovskites. The PL spectra reveal the fact that energy transfers from larger band gap to smaller band gap quasi-2D perovskites.¹³ To quantitatively evaluate the emission intensity, the PLQY is measured. As shown in Fig. 2b, for thin film PBABr/CsPbBr_{0.6}I_{2.4}/PETOx, the PLQY increased remarkably to 91%, over 5 times



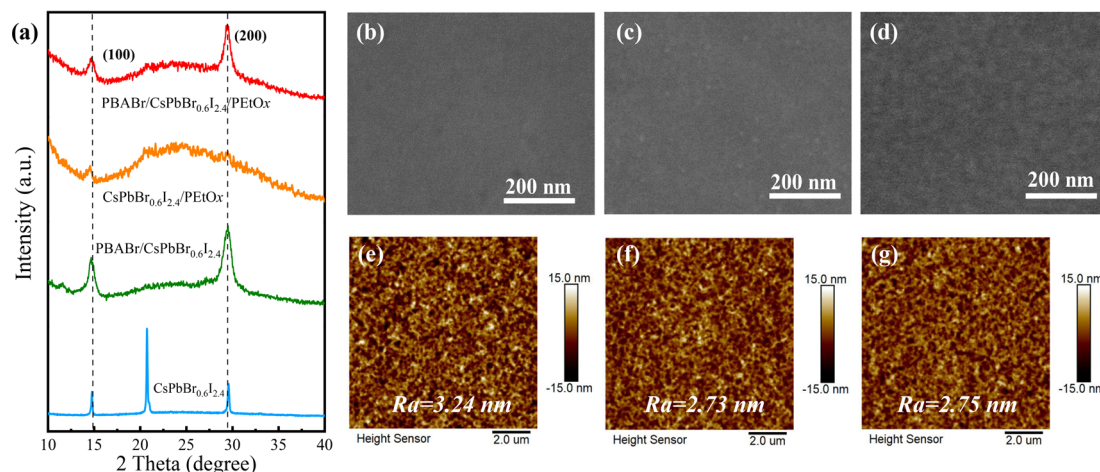


Fig. 1 (a) Powder X-ray diffraction patterns of CsPbBr_{0.6}I_{2.4} thin films with different additives on glass substrates. (b–d) SEM images, and (e–g) AFM images showing the surface morphologies of CsPbBr_{0.6}I_{2.4} thin films with different additives at the same annealing temperature. From left to right: PBABr/CsPbBr_{0.6}I_{2.4}, CsPbBr_{0.6}I_{2.4}/PEtOx and PBABr/CsPbBr_{0.6}I_{2.4}/PEtOx.

higher than that of thin film PBABr/CsPbBr_{0.6}I_{2.4}. Meanwhile, the environmental stabilities of CsPbBr_{0.6}I_{2.4} thin films with different additives were investigated. The moisture stability test was

performed under high humidity conditions (temperature = 298 K, relative humidity RH = 50%) without encapsulation, and the PL spectra were continuously monitored in the process of

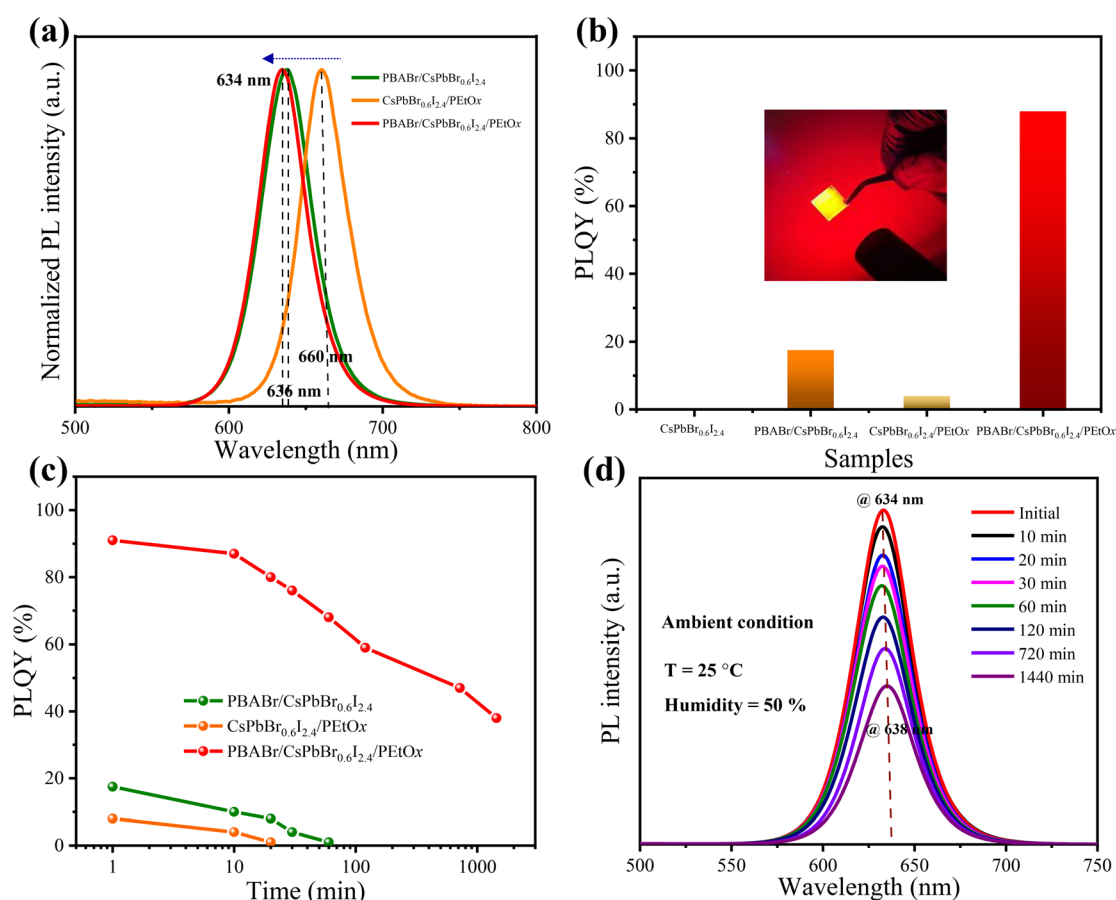


Fig. 2 Optical properties of CsPbBr_{0.6}I_{2.4} thin films with different additives, (a) PL spectra. (b) PLQYs, inset shows the photograph of the 91% PLQY perovskite film under 365 nm UV light irradiation. (c) Stability test of CsPbBr_{0.6}I_{2.4} thin films with different additives under ambient conditions (temperature = 298 K, RH = 50%): time-dependent PLQYs, excitation wavelength: 365 nm. (d) Time-dependent PL spectra of thin film PBABr/CsPbBr_{0.6}I_{2.4}/PEtOx.



aging tests. As exhibited in Fig. 2c, the PLQY of thin films PBABr/CsPbBr_{0.6}I_{2.4} and CsPbBr_{0.6}I_{2.4}/PETOx gradually decreased with time, exhibiting a nearly total (~100%) emission degradation. In comparison, for sample PBABr/CsPbBr_{0.6}I_{2.4}/PETOx, the PLQY can maintain over 40% of the initial emission level after the 24 hours aging test without encapsulation. It is also noteworthy that the peak wavelength and spectral profile of the PL spectra remained almost unchanged over the entire test shown in Fig. 2d. The corresponding PLQYs of the PBABr/CsPbBr_{0.6}I_{2.4}/PETOx composite films with different concentrations of PETOx were measured and are shown in Fig. S4a (ESI[†]). The PLQY increased with an increasing PETOx concentration of up to 20%, showing a maximum PLQY of 91%; further increasing the PETOx concentration resulted in a drop of PLQY. The decrease of PLQY may be due to the increase in the crystal size as revealed by SEM (Fig. S4c, ESI[†]), which leads to a phase separation between the polymer and perovskite phases at higher polymer blending ratios.⁹ We have also tested the stability of perovskite films with different concentrations of PETOx shown in Fig. S4b (ESI[†]). Compared to composite perovskite films with 20% PETOx, PLQY could only maintain 15% of the initial emission level after 24 h aging test for the sample containing 30% PETOx. The results show that, as a protective agent, an appropriate PETOx network could provide physical isolation to protect the quasi-2D perovskite films from high humidity, resulting in improved environment stability.

The carrier recombination dynamics play a crucial role in emission behavior. In perovskites, the excited charge carrier dynamics upon photoexcitation undergo decoherence, thermalization, polaron formation, and cooling in the conduction band in the fast timescale of 1 ps, followed by different recombination pathways that relax the carriers to the valence band,¹⁴ as illustrated in Fig. S5 (ESI[†]). The radiative efficiency η , or the PLQY, could be expressed by the following equation:¹⁵

$$\eta = \frac{k_2 n^2}{k_1 n + k_2 n^2 + k_3 n^3} \quad (1)$$

where n is the carrier density, k_1 is the mono-molecular recombination constant, representing trap-assisted recombination, k_2 is the bi-molecular recombination constant, representing radiative recombination, and k_3 is the tri-molecular recombination constant, representing the non-radiative Auger recombination.¹⁶ As shown in eqn (1), the radiative efficiency η is dependent on the three recombination constants (k_1 , k_2 , and k_3) and carrier density (n). In the case of extremely low carrier density, trap-assisted recombination dominates and largely determines the PLQY. As the carrier density increases, the radiative recombination starts to compete over trap-assisted recombination and gradually dominates, thus enhancing the PLQY. Under the situation of extremely high carrier density, Auger recombination becomes dominant and decreases the PLQY.^{15a} Therefore, enhancing the radiative recombination rate (k_{rad} , larger k_2) and suppressing the non-radiative recombination rate (k_{nonrad} , smaller k_1 and k_3) could increase the emissive efficiency.

To quantitatively analyze the recombination dynamics of PBABr/CsPbBr_{0.6}I_{2.4} and PBABr/CsPbBr_{0.6}I_{2.4}/PETOx thin films, we first investigated the k_1 through TRPL measurements under

extremely low excitation power (Fig. S6, ESI[†]), where the trap-assisted recombination dominates and high-order recombination contribution is inappreciable.¹⁷ As calculated, the thin film PBABr/CsPbBr_{0.6}I_{2.4}/PETOx ($k_1: 0.21 \times 10^7 \text{ s}^{-1}$) possesses a lower trap-assisted non-radiative recombination rate than thin film PBABr/CsPbBr_{0.6}I_{2.4} ($k_1: 4.7 \times 10^7 \text{ s}^{-1}$), attributable to the better interface passivation as PETOx is introduced.¹⁸ To further verify the above conclusion, we directly characterize the defect densities using space-charge limited current measurement with a device structure of ITO/PEDOT/perovskite/MoO₃/Ag (Fig. S7, ESI[†]). As expected, thin film PBABr/CsPbBr_{0.6}I_{2.4}/PETOx shows a relatively lower defect density of $1.3 \times 10^{16} \text{ cm}^{-3}$ compared to thin film PBABr/CsPbBr_{0.6}I_{2.4} ($8.6 \times 10^{16} \text{ cm}^{-3}$).¹⁹

Fig. 3 shows the recombination dynamics of CsPbBr_{0.6}I_{2.4} thin films with or without PETOx additives under various excitation powers. In Fig. 3a, with 400 nm excitation, ground state bleaching (GSB) signals were observed at 448 nm ($n = 2$) and 540 nm ($n = 3$), demonstrating the generation of excited states in the $n = 2$ and $n = 3$ domains for the 0.6PBABr-CsPbBr_{0.6}I_{2.4}-0% PETOx thin film. In contrast, for the thin film with 20% PETOx, the 540 nm ($n = 3$) signals became weak, and the 448 nm ($n = 2$) signal disappeared, while only the signals at 600 nm ($n \geq 4$) remained (Fig. 3b). And the initial TA bleach signals plotted over pump power for perovskite thin films are shown in Fig. S8 (ESI[†]), which indicate that they are in the unsaturated absorption region.

Subsequently, the charge-carrier recombination kinetics can be quantitatively described by the following equation:²⁰

$$-\frac{dn(t)}{dt} = k_1 \cdot n(t) + k_2 \cdot n(t)^2 + k_3 \cdot n(t)^3 \quad (2)$$

The k_2 and k_3 can be extracted by fitting TA spectra under various excitation fluences with eqn (2) (Fig. 3c-f).²¹ The fitting results are summarized in Table 1 and the calculation details can be referred to from the previous reports generated by Du *et al.*²² The bi-molecular recombination constant k_2 of PBABr/CsPbBr_{0.6}I_{2.4}/PETOx is about 8 times higher than that of PBABr/CsPbBr_{0.6}I_{2.4}, indicating enhanced radiative recombination rate with stronger carrier confinement in the sample with PETOx additives.

As expected, the measured PLQY of PBABr/CsPbBr_{0.6}I_{2.4}/PETOx (91%) is indeed higher than that of PBABr/CsPbBr_{0.6}I_{2.4} (18.5%) under a moderate excitation fluence. We note that the Auger recombination constant k_3 of PBABr/CsPbBr_{0.6}I_{2.4}/PETOx is also about 5 times higher than that of PBABr/CsPbBr_{0.6}I_{2.4}, which are attributed to the smaller CsPbBr_{0.6}I_{2.4} nano-grains and stronger confinement.^{15b} Therefore, the addition of the PETOx polymer can not only reduce the trap-assisted recombination rate k_1 but also significantly increase the bi-molecular recombination rate k_2 , which is promising to improve the PLQY of the perovskite thin film. On the basis of the above discussion, the enhanced PLQY can be attributed to the suppressed non-radiative loss as well as the remarkably increased radiative recombination rate by PETOx additive engineering. Moreover, the results demonstrate the stability of perovskite thin film PBABr/CsPbBr_{0.6}I_{2.4}/PETOx in air. This is evident that PETOx



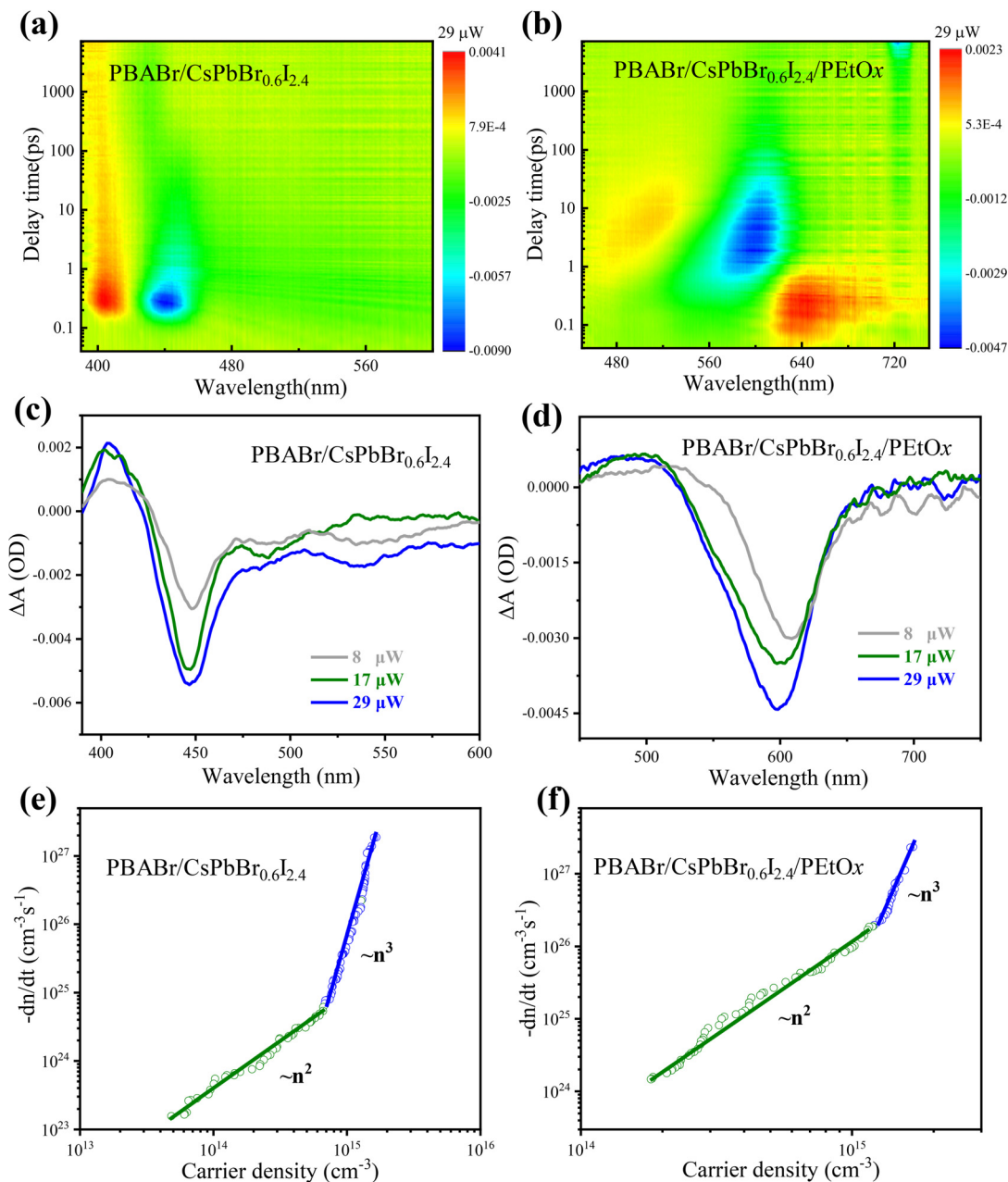


Fig. 3 The recombination dynamics of CsPbBr_{0.6}I_{2.4} thin films with different additives. The pseudo-color maps of thin films PBABr/CsPbBr_{0.6}I_{2.4} (a) and PBABr/CsPbBr_{0.6}I_{2.4}/PEtOx (b) under an excitation power of 29 μW. The transient absorption spectra of thin film PBABr/CsPbBr_{0.6}I_{2.4} (c), PBABr/CsPbBr_{0.6}I_{2.4}/PEtOx (d) under 1 ps delay time with various excitation densities. (e and f) The relationship between carrier recombination decay rates and carrier density.

Table 1 The fitted results of recombination rate constants for perovskite films with different additives

Sample	k_1 (s ⁻¹)	k_2 (cm ³ s ⁻¹)	k_3 (cm ⁶ s ⁻¹)
PBABr/CsPbBr _{0.6} I _{2.4}	4.7×10^7	1.8×10^{-10}	1.3×10^{-27}
PBABr/CsPbBr _{0.6} I _{2.4} /PEtOx	0.21×10^7	9.4×10^{-10}	6.1×10^{-27}

The k_1 is extracted from time-resolved PL under the low excitation fluence, and k_2 and k_3 are obtained from the global fitting of recombination rates–carrier density curves.

treated perovskite films with pure-red emission are compatible for practical optoelectronic domains even in an air environment.

The principle of the laser direct-write patterning method used in this work is based on steering the pulsed and focused laser beam by two orthogonal scanning mirrors driven by galvanometers. The material of the perovskite thin film is selectively removed by the laser. The pre-programmed removal pattern is realized by the two scanning mirrors combined with on/off control of the laser pulse. The detailed laser writing setup is schematically shown in Fig. S9 (ESI†). Considering the significance of wafer-scale fabrication of perovskite fluorescence



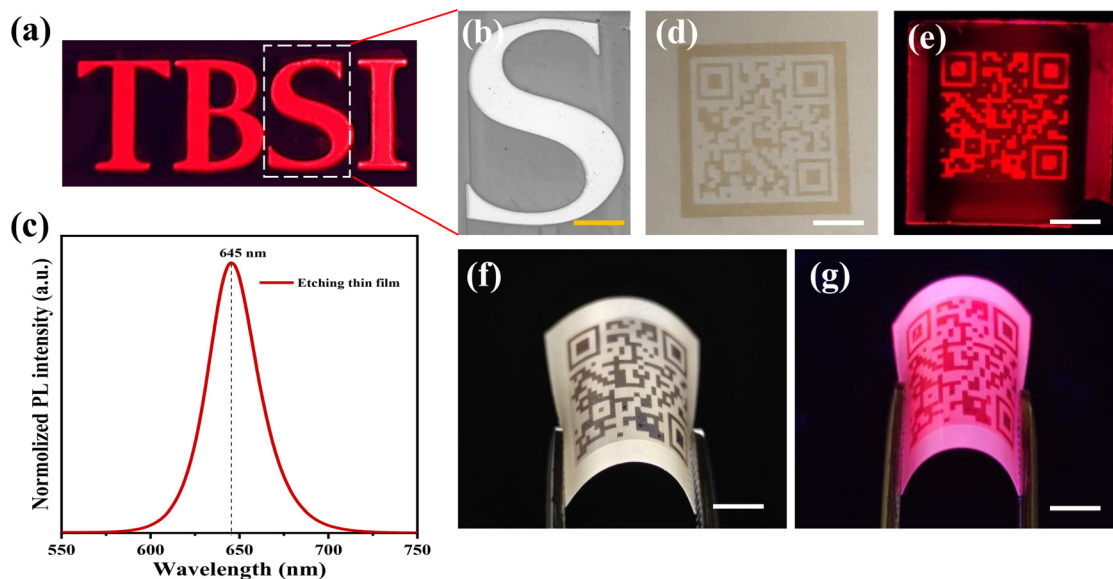


Fig. 4 Perovskite fluorescence patterns on various substrates *via* laser etching. (a) Fluorescence image of the laser-etched macroscopic letters “TBSI” in the perovskite film. (b) Enlarged SEM image of the letter “S”. The scale bar of (b) is 500 μm . (c) PL spectra of the perovskite fluorescence patterns after laser etching. (d and e) Two-dimensional code of “Tsinghua University”. The scale bars are 2 mm. (f and g) Digital photographs and fluorescence images of large-area flexible perovskite bended patterns on PC substrates using the laser direct-write patterning method. The scale bars are 2 mm.

patterns for various light-emitting application, we prepared large-area fluorescent perovskite thin film patterns with PLQY as high as 56% on a glass substrate by laser direct-write patterning. Due to the high-quality and uniform surface of the perovskite films, we can realize an ultrafast-laser direct patterning process without mask or any other complex lift-off procedure.²³ By optimizing the pulse duration, repetition rate, and pulse energy, a series of patterns can be obtained. As shown in Fig. 4a, the fluorescence image of the macroscopic letters “TBSI” with bright pure-red emission in millimeter scale was prepared. The enlarged SEM images confirmed that the perovskite thin film patterns exhibited excellent homogeneity, stability and reproducibility (Fig. 4b). The photoluminescence peak position is located at 645 nm (Fig. 4c) after the laser etching process, showing pure-red emission. It is noteworthy that the PL spectrum is red-shifted slightly. The representative XRD patterns of the perovskite films before and after laser etching are shown in Fig. S10 (ESI[†]). Strong (100) and (200) diffraction peaks were observed, indicating that both of the perovskite films have cubic structures. After laser etching, the two XRD peaks become narrower, suggesting the growth of $\text{CsPbBr}_{0.6}\text{I}_{2.4}$ crystals. In addition, a new peak located at 20.8° (marked by stars) appeared, which correspond to the δ phase of CsPbI_3 .²⁴ Furthermore, after laser etching, the crystal size in the perovskite film became enlarged compared with the pristine one, shown in the SEM images (Fig. S11, ESI[†]). The conclusion can be drawn that the red shift of the PL spectrum was related to the crystal size change caused by laser etching heating.²⁵

In addition, this direct laser patterning technique can be used to prepare any well-designed patterns. Benefiting from the substantially enhanced emission performance and material stability after PETox treatment, the resulting perovskite thin films may act as a smart and security pattern in anti-counterfeiting applications. Thus, a two-dimensional code was prepared (Fig. 4d

and e). Through this direct laser patterning method, anti-counterfeiting information can be hidden, and it is difficult for a counterfeiter to imitate in a printed invisible pattern. Under UV light irradiation, the appearance of a bright red two-dimensional code containing the information of “Tsinghua University” can be clearly seen. The processes of encrypting and decrypting were implemented using UV light on/off as a switch. It implied a promising application in multidimensional information encoding and anticounterfeiting.

Compared with microfabrication techniques,^{23,26} this laser direct patterning method is efficient and inexpensive. All of these patterns were transparent and stable in the ambient environment. Meanwhile, our approach can be extended to other types of metal halide perovskites such as perovskite quantum dots (QDs) and vacuum-deposited perovskites, as well as flexible substrates such as polydimethylsiloxane (PDMS), polycarbonate (PC), polyethylene terephthalate (PET) films, *etc.* Herein, without any other complex lift-off procedure or being transferred to flexible substrates, we obtained large-area fluorescence flexible patterns *via* the laser direct-write patterning method directly on the PC substrate. As shown in Fig. 4f and g, the fluorescence images of the complicated patterns of two-dimensional code of Tsinghua University were prepared, showing bright red fluorescence under UV light. These patterns could be bended to different angles, showing good flexibility. The above results indicated that these high PLQY perovskite thin films *via* the laser direct-write patterning method show diverse potential for wearable light-emitting devices and flexible panel display applications.²⁷

Conclusions

In summary, significant enhancement of the PLQY and stability in quasi-2D perovskite thin films was achieved by PETox



engineering *via* a one-step method, where the PLQY was boosted to 91% from the initial value of 18.5%. Time-resolved optical measurements and femtosecond-transient absorption revealed that PEtOx treated quasi-2D perovskites induced a remarkably suppressed non-radiative loss by 5 times and a promoted radiative recombination rate by 8 times, which together contribute to the PL enhancement. Moreover, we have succeeded in developing a high resolution, large-area laser etching patterning method to pattern perovskite thin films. Taking advantage of the uniformity of the perovskite thin film and the generic etching approach, various pure-red single-color patterns have been successfully fabricated. Compared with microfabrication techniques, this etching method is efficient and economic. It opens opportunities to fabricate all laser etching perovskite optoelectronic devices and may extend for exploring other types of materials for a wide range of applications. Further study should continue to improve device performance by balancing the high PL and efficient carrier injection *via* additive optimization and further improving device stability.

Experimental section

Materials

Cesium iodide (CsI, 99.999%), cesium bromide (CsBr, 99.999%) and lead bromide (PbBr₂, 99.999%) were purchased from Sigma Aldrich; lead iodide (PbI₂, 99.999%) was bought from Xi'an Polymer Light Technology Crop; poly(2-ethyl-2-oxazoline) (PEtOx) polymer with average molecular weight of 50 000 was purchased from Sigma Aldrich; phenylbutylamine bromide (PBABr) was purchased from Xi'an Polymer Light Technology Crop; anhydrous dimethyl sulfoxide (DMSO, ≥99.9%) was purchased from Sigma-Aldrich; poly[bis(4-phenyl)(4-butylphenyl)amine] (poly-TPD) purchased from American Dye Source (Canada) was utilized; ZnMgO/ethanol (50 mg mL⁻¹) solution was purchased from Guangdong Poly Optoelectronics Crop. All materials and reagents were used as received without further purification.

Preparation of quasi-2D perovskite thin films

CsI and PbI₂ were dissolved in DMSO with a molar ratio of 1 : 1 to form a 0.25 M CsPbI₃ precursor solution. CsBr and PbBr₂ were dissolved in DMSO with a molar ratio of 1 : 1 to form a 0.25 M CsPbBr₃ precursor solution. CsPbBr_{0.6}I_{2.4} solutions were fabricated by mixing CsPbI₃ and CsPbBr₃ precursor solutions with a 4 : 1 volume ratio. Organic salt PBABr was dissolved in DMSO at a concentration of 0.5 M. PEtOx was dissolved in DMSO with a concentration of 100 mg mL⁻¹. Appropriate amounts of PEtOx with a weight ratio of 20% ($w_{\text{PEtOx}} : w_{\text{Pb}} = 20\%$) was added to the CsPbBr_{0.6}I_{2.4} solutions to gain CsPbBr_{0.6}I_{2.4}/PEtOx. The weight ratio of PEtOx to CsPbBr_{0.6}I_{2.4} solutions remained as 20% in all the fabricated perovskite films while the molar ratio of PBABr was varied. Right before spin coating, the precursor solutions were stirred overnight and filtered by a 0.22 μm polytetrafluoroethylene (PTFE) syringe filter. The mixture precursor was spun-cast upon glass or flexible substrates at

4000 rpm for 45 s, followed by thermal annealing at a temperature of 110 °C for 10 min. A ~50 nm thick quasi-2D perovskite/PETox composite thin film was obtained.

Characterization of perovskite thin films

XRD data were obtained using a D8 advance X-ray diffraction instrument with Cu Kα source in the range of 10°–50°. The photoluminescence (PL) spectra and photoluminescence quantum yields (PLQYs) of perovskite thin films were obtained with an XPQY spectrometer (Xipu Optoelectronics Crop) under the irradiation of the 365 nm laser. Emission decay kinetics with Time Resolution Photoluminescence (TRPL) spectra were obtained using an Edinburgh FS5 fluorescence spectrometer at room temperature using time-correlated single photon counting (TCSPC; 1024 channels; 500 ns window) with data collection for 3000 counts. For transient absorption (TA) measurements, femtosecond laser pulses of an 800 nm fundamental beam (1 kHz repetition rate, 35 fs pulse width) were produced using a Ti:sapphire oscillator seeded regenerative amplifier (Spectra Physics, Spitfire Ace). Part of the 800 nm laser beam passed through a BBO crystal to generate a 400 nm beam by second harmonic generation, which served as a narrowband pump. The other part was focused onto a 1 mm sapphire plate to generate a white-light supercontinuum probe. Both the pump and probe pulses were directed into a commercial TA spectrometer (Helios, Ultrafast Systems). The surface morphologies of the perovskite thin films in the sample structure of the ITO/ZnMgO/perovskite were investigated with a Hitachi SU8010 cold field emission scanning electron microscope (SEM). The surface roughness and thickness of different perovskite thin films were measured using an atomic force microscope (AFM).

Laser etching characterization

After the preparation of films *via* spin coating and thermal annealing, we use a direct laser to etch out the excess film and obtain certain patterns. We use a direct UV laser produced by 3K Laser Technology Co., Ltd, with a wavelength of 355 nm, a maximum power of 3 W, and a laser frequency of 30 kHz. The pattern required for etching is filled with a straight line with a spacing of 0.01 mm, and the laser sweeps through the surface of the film at a speed of 500 mm s⁻¹. Flexible laser direct-write patterning patterns were obtained using a polycarbonate (PC) plastic substrate. The PL images of the patterned perovskite film were collected by confocal fluorescence microscopy. It is noted that all the laser direct-write patterning procedures are conducted in an air environment outside the glovebox without encapsulation.

Author contributions

P. L., B. Y. Y. and W. Q. C. contributed equally to this work. P. L. wrote the manuscript, carried out the experiments of device fabrication, performance characterization and data analysis; B. Y. Y. and X. Y. Z. carried out the experiments of laser direct patterning; W. Q. C. helped to complete the idea and achieve



the TA results; X. X. Y. assisted in the photoluminescence measurements; K. C. assisted in the exploration of laser etching experiments; G. D. W., W. W. D. and Y. Y. Z. led the project and supervised the research. All authors contributed to revising the manuscript.

Conflicts of interest

The authors declare no competing financial interest.

Acknowledgements

We acknowledge the funding support from the National Natural Science Foundation of China (Grant Numbers: 52027817, 11932009), the Science and Technology Planning Project of Shenzhen Municipality (Grant number: JCYJ20200109144615514), and the Shenzhen Science and Technology Innovation Committee (Grant number: RCBS20210706092343014).

References

- 1 S. Kalytchuk, Y. Wang, K. Polakova and R. Zboril, *ACS Appl. Mater. Interfaces*, 2018, **10**, 29902–29908.
- 2 J. Andres, R. D. Hersch, J. E. Moser and A. S. Chauvin, *Adv. Funct. Mater.*, 2014, **24**, 5029–5036.
- 3 (a) S. Bai, P. Da, C. Li, Z. Wang, Z. Yuan, F. Fu, M. Kawecki, X. Liu, N. Sakai, J. T. Wang, S. Huettner, S. Buecheler, M. Fahlman, F. Gao and H. J. Snaith, *Nature*, 2019, **571**, 245–250; (b) C. C. Zhang, Z. K. Wang, S. Yuan, R. Wang, M. Li, M. F. Jimoh, L. S. Liao and Y. Yang, *Adv. Mater.*, 2019, **31**, e1902222; (c) S.-H. Jeong, H. Cho, M.-H. Park, Y.-H. Kim, C. Wolf, C.-L. Lee, J. H. Heo, A. Sadhanala, N. Myoung, S. Yoo, S. H. Im, R. H. Friend and T.-W. Lee, *Science*, 2015, **350**, 1222–1225; (d) B. Zhao, S. Bai, V. Kim, R. Lamboll, R. Shivanna, F. Auras, J. M. Richter, L. Yang, L. Dai, M. Alsari, X.-J. She, L. Liang, J. Zhang, S. Lilliu, P. Gao, H. J. Snaith, J. Wang, N. C. Greenham, R. H. Friend and D. Di, *Nat. Photonics*, 2018, **12**, 783–789; (e) Y. Liu, F. Li, C. Perumal Veeramalai, W. Chen, T. Guo, C. Wu and T. W. Kim, *ACS Appl. Mater. Interfaces*, 2017, **9**, 11662–11668.
- 4 (a) F. Zhang, Z. Shi, S. Li, Z. Ma, Y. Li, L. Wang, D. Wu, Y. Tian, G. Du, X. Li and C. Shan, *ACS Appl. Mater. Interfaces*, 2019, **11**, 28013–28022; (b) Y. L. Tong, Y. W. Zhang, K. Ma, R. Cheng, F. Wang and S. Chen, *ACS Appl. Mater. Interfaces*, 2018, **10**, 31603–31609.
- 5 (a) J. S. Park, J. Kyhm, H. H. Kim, S. Jeong, J. Kang, S. E. Lee, K. T. Lee, K. Park, N. Barange, J. Han, J. D. Song, W. K. Choi and I. K. Han, *Nano Lett.*, 2016, **16**, 6946–6953; (b) Y. L. Kong, I. A. Tamargo, H. Kim, B. N. Johnson, M. K. Gupta, T. W. Koh, H. A. Chin, D. A. Steingart, B. P. Rand and M. C. McAlpine, *Nano Lett.*, 2014, **14**, 7017–7023; (c) B. Bao, M. Li, Y. Li, J. Jiang, Z. Gu, X. Zhang, L. Jiang and Y. Song, *Small*, 2015, **11**, 1649–1654.
- 6 X. Yang, J. Wu, T. Liu and R. Zhu, *Small Methods*, 2018, **2**, 1800110.
- 7 (a) Y. Liu, F. Li, L. Qiu, K. Yang, Q. Li, X. Zheng, H. Hu, T. Guo, C. Wu and T. W. Kim, *ACS Nano*, 2019, **13**, 2042–2049; (b) L. Shi, L. Meng, F. Jiang, Y. Ge, F. Li, X. G. Wu and H. Zhong, *Adv. Funct. Mater.*, 2019, **29**, 1903648; (c) D. Lohse, *Annu. Rev. Fluid Mech.*, 2022, **54**, 349–382.
- 8 (a) X. Hu, Z. Huang, X. Zhou, P. Li, Y. Wang, Z. Huang, M. Su, W. Ren, F. Li, M. Li, Y. Chen and Y. Song, *Adv. Mater.*, 2017, **29**, 1703236; (b) S. Hou, Y. Guo, Y. Tang and Q. Quan, *ACS Appl. Mater. Interfaces*, 2017, **9**, 18417–18422.
- 9 W. Cai, Z. Chen, Z. Li, L. Yan, D. Zhang, L. Liu, Q. H. Xu, Y. Ma, F. Huang, H. L. Yip and Y. Cao, *ACS Appl. Mater. Interfaces*, 2018, **10**, 42564–42572.
- 10 X. B. Cao, C. L. Li, L. L. Zhi, Y. H. Li, X. Cui, Y. W. Yao, L. J. Ci and J. Q. Wei, *J. Mater. Chem. A*, 2017, **5**, 8416–8422.
- 11 G. E. Eperon, G. M. Paternò, R. J. Sutton, A. Zampetti, A. A. Haghighirad, F. Cacialli and H. J. Snaith, *J. Mater. Chem. A*, 2015, **3**, 19688–19695.
- 12 X. Liu, J. Wu, Q. Guo, Y. Yang, H. Luo, Q. Liu, X. Wang, X. He, M. Huang and Z. Lan, *J. Mater. Chem. A*, 2019, **7**, 11764–11770.
- 13 M. Yuan, L. N. Quan, R. Comin, G. Walters, R. Sabatini, O. Voznyy, S. Hoogland, Y. Zhao, E. M. Bearegard, P. Kanjanaboos, Z. Lu, D. H. Kim and E. H. Sargent, *Nat. Nanotechnol.*, 2016, **11**, 872–877.
- 14 L. M. Herz, *Annu. Rev. Phys. Chem.*, 2016, **67**, 65–89.
- 15 (a) X. K. Liu, W. Xu, S. Bai, Y. Jin, J. Wang, R. H. Friend and F. Gao, *Nat. Mater.*, 2021, **20**, 10–21; (b) Z. Chen, Z. Li, C. Zhang, X.-F. Jiang, D. Chen, Q. Xue, M. Liu, S. Su, H.-L. Yip and Y. Cao, *Adv. Mater.*, 2018, **30**, 1801370.
- 16 (a) Y. Yamada, T. Nakamura, M. Endo, A. Wakamiya and Y. Kanemitsu, *J. Am. Chem. Soc.*, 2014, **136**, 11610–11613; (b) C. Wehrenfennig, G. E. Eperon, M. B. Johnston, H. J. Snaith and L. M. Herz, *Adv. Mater.*, 2014, **26**, 1584–1589; (c) L. Lei, Q. Dong, K. Gundogdu and F. So, *Adv. Funct. Mater.*, 2021, **31**, 2010144.
- 17 G. Xing, B. Wu, X. Wu, M. Li, B. Du, Q. Wei, J. Guo, E. K. Yeow, T. C. Sum and W. Huang, *Nat. Commun.*, 2017, **8**, 14558.
- 18 Y. Ling, L. Tan, X. Wang, Y. Zhou, Y. Xin, B. Ma, K. Hanson and H. Gao, *J. Phys. Chem. Lett.*, 2017, **8**, 3266–3271.
- 19 X. Shen, Y. Zhang, S. V. Kershaw, T. Li, C. Wang, X. Zhang, W. Wang, D. Li, Y. Wang, M. Lu, L. Zhang, C. Sun, D. Zhao, G. Qin, X. Bai, W. W. Yu and A. L. Rogach, *Nano Lett.*, 2019, **19**, 1552–1559.
- 20 Y. Jiang, M. Cui, S. Li, C. Sun, Y. Huang, J. Wei, L. Zhang, M. Lv, C. Qin, Y. Liu and M. Yuan, *Nat. Commun.*, 2021, **12**, 336.
- 21 J. M. Richter, M. Abdi-Jalebi, A. Sadhanala, M. Tabachnyk, J. P. H. Rivett, L. M. Pazos-Outon, K. C. Godel, M. Price, F. Deschler and R. H. Friend, *Nat. Commun.*, 2016, **7**, 13941.
- 22 P. Du, J. Li, L. Wang, L. Sun, X. Wang, X. Xu, L. Yang, J. Pang, W. Liang, J. Luo, Y. Ma and J. Tang, *Nat. Commun.*, 2021, **12**, 4751.
- 23 C. Zou, C. Chang, D. Sun, K. F. Bohringer and L. Y. Lin, *Nano Lett.*, 2020, **20**, 3710–3717.



- 24 B. Han, B. Cai, Q. Shan, J. Song, J. Li, F. Zhang, J. Chen, T. Fang, Q. Ji, X. Xu and H. Zeng, *Adv. Funct. Mater.*, 2018, **28**, 1804285.
- 25 J. A. Sichert, Y. Tong, N. Mutz, M. Vollmer, S. Fischer, K. Z. Milowska, R. Garcia Cortadella, B. Nickel, C. Cardenas-Daw, J. K. Stolarczyk, A. S. Urban and J. Feldmann, *Nano Lett.*, 2015, **15**, 6521–6527.
- 26 (a) D. N. Minh, S. Eom, L. A. T. Nguyen, J. Kim, J. H. Sim, C. Seo, J. Nam, S. Lee, S. Suk, J. Kim and Y. Kang, *Adv. Mater.*, 2018, **30**, 1802555; (b) Z. Gu, Z. Huang, X. Hu, Y. Wang, L. Li, M. Li and Y. Song, *ACS Appl. Mater. Interfaces*, 2020, **12**, 22157–22162.
- 27 (a) Z. Wu, J. Chen, Y. Mi, X. Sui, S. Zhang, W. Du, R. Wang, J. Shi, X. Wu, X. Qiu, Z. Qin, Q. Zhang and X. Liu, *Adv. Opt. Mater.*, 2018, **6**, 1800674; (b) Q. Zhou, Z. Bai, W. G. Lu, Y. Wang, B. Zou and H. Zhong, *Adv. Mater.*, 2016, **28**, 9163–9168.

